Damping performance of finite microperforated plates using multi-size and spatial distributions of perforations

Lucie Gallerand, Mathias Legrand, Thomas Dupont, Raymond Panneton, Philippe Leclaire

▶ **To cite this version:**

Lucie Gallerand, Mathias Legrand, Thomas Dupont, Raymond Panneton, Philippe Leclaire. Damping performance of finite microperforated plates using multi-size and spatial distributions of perforations. Applied Acoustics, 2024, 10.1016/j.apacoust.2024.110041 . hal-04122565v3

HAL Id: hal-04122565
https://hal.science/hal-04122565v3

Submitted on 2 May 2024

HAL is a multi-disciplinary open access archive for the deposit and dissemination of scientific research documents, whether they are published or not. The documents may come from teaching and research institutions in France or abroad, or from public or private research centers.

L'archive ouverte pluridisciplinaire **HAL**, est destinée au dépôt et à la diffusion de documents scientifiques de niveau recherche, publiés ou non, émanant des établissements d'enseignement et de recherche français ou étrangers, des laboratoires publics ou privés.

Distributed under a Creative Commons Attribution 4.0 International License

Damping performance of finite microperforated plates using multi-size and spatial distributions of perforations

Lucie Gallerand[a], Mathias Legrand[b], Thomas Dupont[a], Raymond Panneton[c], Philippe Leclaire[d]

[a] *Department of Mechanical Engineering, École de technologie supérieure, Montréal, Canada*
[b] *Department of Mechanical Engineering, McGill University, Montréal, Canada*
[c] *CRASH-UdeS, Department of Mechanical Engineering, Université de Sherbrooke, Sherbrooke, Canada*
[d] *DRIVE EA1859, Université de Bourgogne Franche-Comté, ISAT, Nevers, France*

In the context of structural dynamics, recent works by the authors showed that microperforations can be used to mitigate vibration. Microperforated plates (MPP) have been shown to exhibit substantial added damping arising from fluid-structure interactions and visco-thermal effects in the boundary layers of the perforations during relative motion between the solid and the fluid contained in the perforations. The added damping reaches a maximum for a characteristic frequency, depending only on the diameter of the perforation. Choosing the diameter of the perforation so that the characteristic frequency coincides with a given natural frequency of the plate reduces the contribution of the associated plate mode. However, the MPP studied had a single set of perforations homogeneously distributed throughout the structure. In this work, it is proposed to extend the added damping to several modes of the plate by using MPP with multi-size perforations and an optimized spatial distribution of these perforations. As an extension of the previous vibratory model of the authors, the dynamics of MPP with perforations of multiple sizes based on a homogenization model is established. In addition, the effect of the spatial distribution of perforations on the additional damping is captured by including a spatially dependent perforation ratio in the model. Experimental measurements on MPP validate the proposed analytical models. The results show that (i) MPP with multiple-size perforations feature a wider effective damping frequency band, and (ii) the added damping is accentuated when the perforations are distributed in the zone of the antinodes of the considered modes. Thus, by combining the two effects, it is possible to achieve MPP that effectively reduce the vibratory responses on several modes.

Keywords: Microperforated plate — Additional damping — Multi-size perforations — Gradients of properties

Contents

1. Introduction

Microperforated plates (MPP) are usually employed as lightweight acoustic absorbers for noise reduction and are regarded as an alternative to conventional porous materials or conventional acoustic resonators.

Email addresses: lucie.gallerand.1@ens.etsmtl.ca (Lucie Gallerand), mathias.legrand@mcgill.ca (Mathias Legrand), thomas.dupont@etsmtl.ca (Thomas Dupont), raymond.panneton@usherbrooke.ca (Raymond Panneton), philippe.leclaire@u-bourgogne.fr (Philippe Leclaire)

Nomenclature

Geometric constants

d	diameter of perforation (mm)
d_k	perforation diameter of subdomain k
h	plate or MPP thickness (mm)
L_x	plate or MPP length in x direction (mm)
L_y	plate or MPP length in y direction (mm)

Macroscopic parameters

α_∞	tortuosity
$\alpha_\infty(x,y)$	spatial tortuosity
$\phi^{(0)}$	perforation ratio
$\phi^{(0)}_{\text{tot}}$	total perforation ratio
$\phi^{(0)}_k$	perforation ratio of subdomain k
$\phi(x,y)$	spatial perforation ratio
$\sigma^{(0)}$	fluid flow resistivity ($\mathrm{N\,s\,m^{-4}}$)
$\sigma^{(0)}_{\text{tot}}$	total fluid flow resistivity ($\mathrm{N\,s\,m^{-4}}$)
$\sigma^{(0)}_k$	fluid flow resistivity of subdomain k ($\mathrm{N\,s\,m^{-4}}$)
$\sigma(x,y)$	spatial fluid flow resistivity ($\mathrm{N\,s\,m^{-4}}$)
ς	$\varsigma = \sigma^{(0)}\phi^{(0)}$ ($\mathrm{N\,s\,m^{-4}}$)
b_{f}	Biot's friction coefficient ($\mathrm{N\,s\,m^{-4}}$)
f_{c}	Characteristic frequency (Hz)

Mechanical parameters

α	Biot's elastic coupling coefficient
η_{s}	Isotropic structural loss factor
μ_{f}	fluid dynamic viscoelasticity ($\mathrm{kg\,m^{-1}\,s^{-1}}$)
ν	Poisson's coefficient
ρ	plate effective density ($\mathrm{kg\,m^{-3}}$)
ρ_{f}	fluid density ($\mathrm{kg\,m^{-3}}$)
ρ_{s}	stucture density ($\mathrm{kg\,m^{-3}}$)
C_ϕ	stiffenss correction factor
D	bending stiffness ($\mathrm{GPa\,mm^3}$)
E	Young's modulus (GPa)
K_{f}	fluid bulk modulus (kPa)
M_{f}	Biot's elastic coefficient ($\mathrm{N\,m^{-2}}$)

Other parameters

L_Y	mobility level
λ	eigenvalue
λ_{mn}	eigenvalue of mode mn
β	real part of λ
β_{mn}	real part of λ_{mn}
γ	imaginary part of λ ($\mathrm{rad\,s^{-1}}$)
γ_{mn}	imaginary part of λ_{mn} ($\mathrm{rad\,s^{-1}}$)
ω	angular frequency ($\mathrm{rad\,s^{-1}}$)
ω_{mn}	angular undamped frequency of mode mn ($\mathrm{rad\,s^{-1}}$)
N	number of degrees-of-freedom (dof) in plate discretization
η_{mn}	modal loss of mode mn
$\Psi_{mn}(x,y)$	modal shape of mode mn
$\mathrm{Ih}(x,y)$	normalized inhomogeneity function
$w_{\text{f}}(x,y,t)$	fluid motion
$w_{\text{s}}(x,y,t)$	solid motion
$w(x,y,t)$	fluid-solid relative motion

MPP can be used in many fields to reduce noise, such as meeting room [1, 14], acoustic coatings in flow ducts [30] or nuclear engines and reactors [29] for example. These simple structures can be safe, environment-friendly and can be made of different materials. They can be designed to be resistant to harsh environments, translucent or biodegradable. MPP transform acoustic energy into heat by exchanges in the viscous and thermal boundary layers near the fluid-solid interface of the microperforations.

The acoustic properties of microperforated plates were investigated through various models, including models based on the Kirchhoff equations [18] and equivalent fluid models such as the Johnson-Allard approach [10, 3]. Vibrations of MPP were also considered with the aim of investigating their influence on the acoustic properties of structures [27, 11, 7][1]. Research was also conducted to improve and extend MPP' acoustic absorption by using different partitioned cavity depths [26] or multi-size perforation [20, 15], i.e., an MPP whose perforations have various diameters. In fact, Kim and Yoon [15] proposed a multi-size microperforation configuration to improve the sound absorption of MPP in a wide frequency band. An equivalent electro-acoustic circuit method was used to explore the sound absorption properties of a perforated panel with microperforated partitions [8, 9]. Qian *et al.* [25] also used an equivalent electro-acoustic circuit method to model multi-size microperforations. They proposed a multi-population genetic algorithm to optimize the design of multi-size MPP absorbers. Theoretical results showed that only a multi-size MPP absorber with grouped perforations can improve the sound absorption capability of MPP. Mosa *et al.* [21] explored the absorption coefficient of an inhomogeneous MPP with multi-cavity depths. Results showed that introducing an inhomogeneous perforation improved the absorption capability of an MPP absorber compared to a homogeneous one. Experimental and numerical studies have also been performed in an acoustic MPP context with multi-size perforation diameters. Miasa *et al.* [20] explored experimentally the sound absorption performance of a microperforated plate with multi-size perforation diameters. The results showed that multi-size MPP absorbers can exhibit high sound absorption over a wider frequency range than uniformly sized MPP. The authors also concluded that in the case of an MPP with multiple perforation diameters, the benefits of each MPP with a single perforation size were

[1] For a more detailed literature review on the acoustics and vibroacoustics of uniform MPP, the reader is refered to the introduction of [13].

combined. Qian and Zhang [24] used finite element analysis to investigate the influence of an MPP with multi-size perforation diameters on the normal incidence sound absorption performance of a parallel MPP absorber. Some authors have also conducted research on the effect of perforation distribution on the sound absorption of MPP. Temiz *et al.* [28] proposed to numerically explore the effect of perforation distribution on sound absorption by assuming that perforations are discrete impedance patches, as proposed in [22, 19]. Although their works focused on MPP sound absorption, they observed that the distribution of perforations on the MPP could have a significant effect on the viscous damping mechanism. Different diameters and perforation arrangements were modelled using the finite element method and then through an experimental study [23]. They observed that the perforation ratio and the perforation position have an influence on the dynamics of the plate.

In addition to acoustics, the structural dynamics of MPP was also explored. A recent work by the authors [13], and based on [16] and [3], has shown, both theoretically and experimentally, that energy dissipation at the fluid-solid interface in the microperforations drives substantial added damping for the structure. Parametric studies have demonstrated the existence of a single characteristic frequency, which depends on the constant diameter of the perforation and the perforation ratio, at which the added damping reaches a maximum. If this characteristic frequency coincides with one natural frequency of a plate, the vibration in the associated mode will be mitigated by the added damping. However, the added damping will be weaker in the other natural modes. Its impact will be all the more limited as their frequencies are further from the characteristic frequency. An MPP with multiple perforation sizes, and thus with multiple characteristic frequencies (one for each perforation diameter), should theoretically have maximum added damping to its modes having a frequency that coincides with one of the characteristic frequencies. Moreover, additional damping capabilities are due to viscous frictions and thermal exchanges in the boundary layers occurring during the motion of the structure. It is therefore expected that more perforations distributed over the areas where the structural displacement is maximum will induce a magnified added damping. The present work proposes to improve and enhance the additional damping presented by microperforations by using multi-size perforation diameters and a spatial distribution of perforations.

In this paper, each section proposes to study a different type of MPP, as listed below:

Section 2 MPP with uniformly distributed perforations of the same diameters corresponding to the reference MPP;

Section 3 MPP with uniformly distributed perforations of different diameters;

Section 4 MPP with non-uniformly distributed perforations of the same diameters;

Section 5 MPP with non-uniformly distributed perforations of different diameters.

For each section, a model and experimental validations are proposed. To this end, it is first proposed to recall in Section 2 the governing equations of the dynamic of a thin MPP saturated by a lightweight fluid, already detailed in [13]. The model used to capture the effect of multi-size perforation diameters in Section 3 is based on a homogenization approach. In Section 4, the spatial distribution of perforations is considered by defining a spatial perforation ratio. Section 5 proposes to combine the two models presented in Section 3 and Section 4. Finally, conclusions are given in Section 6.

2. MPP: Uniform distribution and single diameter

2.1. Vibration model

The previous work [13] by the authors developed a vibration model of a finite-size MPP of dimensions $L_x \times L_y \times h$, as illustrated in Figure 1, obtained by identifying the MPP with a porous plate and using an alternative form of the Biot's theory [4, 16]. It is used again in the present work, but multi-size and spatially distributed microperforations are considered in Sections 3 to 5. In this model, in-plane displacements are ignored and only the normal displacement is accounted for. The MPP is regarded as a homogeneous plate excited by an external load of the form $f_{\text{ext}}(x, y, t)$. Following a low-frequency assumption, the dynamic response of the MPP saturated by a light fluid is the solution of the two coupled governing equations [13]

$$h(\rho \ddot{w}_{\text{s}}(x, y, t) + \rho_{\text{f}} \ddot{w}(x, y, t)) + \Big(D + \frac{\alpha^2 M_{\text{f}} h^3}{12}\Big)\nabla^4 w_{\text{s}}(x, y, t) = f_{\text{ext}}(x, y, t), \tag{1a}$$

$$\Big(\rho_{\text{f}} \ddot{w}_{\text{s}}(x, y, t) + \frac{\rho_{\text{f}} \alpha_\infty}{\phi^{(0)}} \ddot{w}(x, y, t)\Big) + \sigma^{(0)} \dot{w}(x, y, t) + \alpha M_{\text{f}} \nabla^2 w_{\text{s}}(x, y, t) = 0, \tag{1b}$$

where ∇ is the vector differential operator so that $\nabla^2(\cdot) = \frac{\partial^2(\cdot)}{\partial x^2} + \frac{\partial^2(\cdot)}{\partial y^2}$ and $\nabla^4(\cdot) = \nabla^2(\cdot)^2$. The relative fluid-solid motion is $w(x, y, t) = \phi^{(0)}(w_{\text{f}}(x, y, t) - w_{\text{s}}(x, y, t))$ with $w_{\text{f}}(x, y, t)$, the fluid displacement, and $w_{\text{s}}(x, y, t)$, the solid displacement, and $\phi^{(0)}$ is the perforation ratio. Note that there was a sign error

in [13] but this had no impact on the results presented. The equation system is corrected in this paper. Equation (1a) models the elastic response of the equivalent non-perforated homogeneous solid plate and Equation (1b), the relative fluid-solid motion in the perforations. The coefficient D in Equation (1a) is

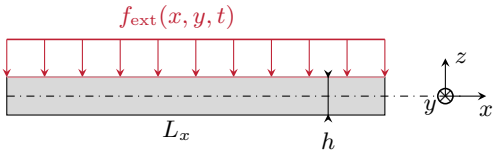

Figure 1: System of coordinates for an equivalent solid plate excited by an external mechanical force along z-axis.

the bending stiffness defined as a function of the plate thickness h, Young's modulus E and Poisson's ratio of the non-perforated structure ν. To capture the effect of microperforations on plate response, Young's modulus E should be adapted to account for the effect of perforations on plate rigidity [6, 13]. The bending stiffness therefore depends on $\phi^{(0)}$ as follows:

$$D = \frac{EC_\phi h^3}{12(1-\nu^2)} \quad \text{with} \quad C_\phi = \frac{(1-\phi^{(0)})^2}{1+(2-3\nu)\phi^{(0)}}. \tag{2}$$

For a vibrating MPP saturated by a lightweight fluid, the elastic modulus of the plate is much greater than that of the fluid, that is, $E \gg M_\text{f}$: accordingly, $D + \frac{\alpha^2 M_\text{f} h^3}{12} \approx D$ in Equation (1) and in the rest of the paper. The density of fluid-solid mixture is captured by $\rho = (1-\phi^{(0)})\rho_\text{s} + \phi^{(0)}\rho_\text{f}$ where ρ_s and ρ_f are the solid and fluid densities, respectively. In Equation (1b), M_f corresponds to the elastic modulus of the equivalent fluid. The dimensionless quantity α characterizes the elastic coupling between the equivalent fluid and the solid. In the context of an MPP saturated by a lightweight fluid, we have $\alpha M_\text{f} \approx K_\text{f}$ [16] where K_f is the bulk modulus of the fluid. With the above assumptions, Equation (1) becomes (temporal and spatial dependencies are omitted)

$$h(\rho_\text{s}(1-\phi^{(0)})\ddot{w}_\text{s} + \rho_\text{f}\phi^{(0)}\ddot{w}_\text{f}) + D\nabla^4 w_\text{s} = f_\text{ext}, \tag{3a}$$

$$\rho_\text{f}((1-\alpha_\infty)\ddot{w}_\text{s} + \alpha_\infty \ddot{w}_\text{f}) + \sigma^{(0)}\phi^{(0)}(\dot{w}_\text{f} - \dot{w}_\text{s}) + K_\text{f}\nabla^2 w_\text{s} = 0. \tag{3b}$$

Some porous parameters used in Biot's theory (airflow resistivity $\sigma^{(0)}$ and tortuosity α_∞) are, for an MPP, functions of the perforation diameter d, perforation ratio $\phi^{(0)}$, plate thickness h, and fluid in the perforations. Thus, the airflow resistivity reads [3]

$$\sigma^{(0)} = \frac{\varsigma}{\phi^{(0)}} \quad \text{with} \quad \varsigma = \frac{32\mu_\text{f}}{d^2} \tag{4}$$

where μ_f is the dynamic viscosity of the fluid. In order to consider the distortion of airflow in the perforations and the fluid-solid interactions between the perforations, an empirical correction is taken into account via the tortuosity as proposed elsewhere [3]. Consequently, the tortuosity is defined as:

$$\alpha_\infty = 1 + B(1 - 1.14\sqrt{\phi^{(0)}}) \quad \text{with} \quad B = \frac{0.48}{h}\sqrt{\pi d^2}. \tag{5}$$

Here, the term in parentheses contains the edge interaction between neighboring perforations. Note that the analytical vibration model presented in this section was validated by experimental measurements on MPP in [13].

2.2. Added damping

An MPP features interactions in viscous and thermal boundary layers associated with fluid-solid interactions, known to induce a non-neglecting additional damping in the plate [13]. This phenomenon reaches a maximum at the characteristic frequency

$$f_\text{c} = \frac{16\mu_\text{f}}{\pi\alpha_\infty\rho_\text{f}d^2} \tag{6}$$

defined from Biot's frequency for porous materials [4, 16]. In Equation (6), f_c depends only on the perforation diameter d and the fluid properties ρ_f and μ_f. The perforation diameter d can be adapted to induce maximum added damping at a resonance frequency, that is, in a way where f_c coincides with a natural frequency of the plate. The additional damping provided by the microperforations is greatest at the characteristic frequency, but also acts in a frequency range centered on f_c.

Figure 2 represents the damping capacities of an aluminum MPP of dimension 490 mm × 570 mm × 1 mm. The MPP is excited by a normal point force $F_{\text{ext}}(x_F, y_F)$ located at $(x_F, y_F) = (80, 70)$ mm on its surface. The level of mobility

$$L_Y = 10 \log\left(\left|\frac{\dot{w}_{\text{s}}(x_R, y_R)}{F_{\text{ext}}(x_F, y_F)}\right|\right) \tag{7}$$

predicted by the model for the MPP at point $(x_R, y_R) = (61.25, 71.25)$ mm is compared to that of a reference plate of the same dimensions without perforations. The perforation diameter of the MPP is set to $d \equiv d_1 = 1.6$ mm in order to induce maximum added damping on the first MPP mode. The perforation ratio is set to $\phi^{(0)} = 10\,\%$. The reduction in vibration and the loss factor at each MPP

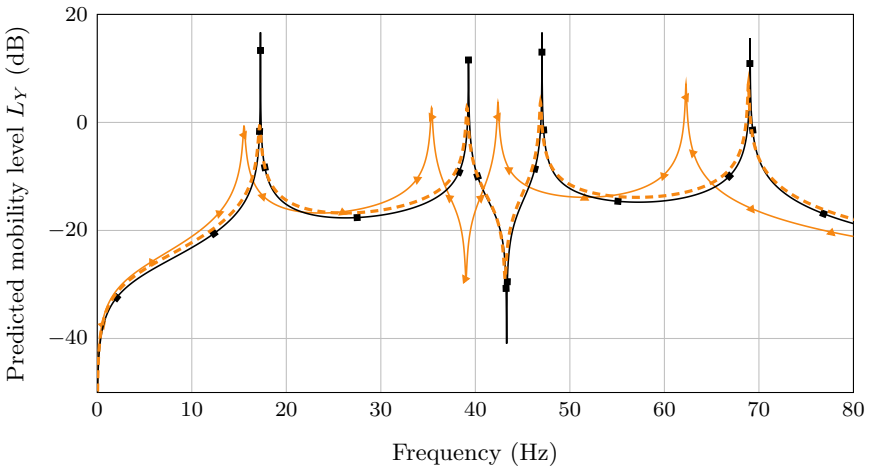

Figure 2: Predicted mobility level of aluminum plates of dimensions 490 mm × 570 mm × 1 mm: (—■—) reference non-perforated plate, (—▲—) MPP with a perforation diameter, denoted d_1, set to induce maximum added damping in the first MPP mode, and (- - -) MPP with the same equivalent stiffness as the reference non-perforated plate and with $d \equiv d_1$ maximizing the added damping on the first MPP mode. Perforation parameters are $d_1 = 1.6$ mm and $\phi^{(0)} = 10\,\%$. Isotropic structural loss factor of aluminum $\eta_{\text{s}} = 10^{-4}$ or 0.01 % is also considered.

resonance frequency are listed in Table 1. The loss factor η_{mn} is related to the modal damping ratio ζ_{mn} by the following expression $\eta_{mn} = 2\zeta_{mn}$ at the eigenfrequency. The modal damping ratio ζ_{mn} is obtained for mode (m, n) after solving Equation (1) via a modal analysis as detailed in [13]. The structural loss factor for aluminum is assumed to be frequency-independent and is set to $\eta_{\text{s}} = 10^{-4}$ or 0.01%. The mobility reduction ΔY_{mn} is determined by the difference in mobility level between the MPP and the reference plate in mode (m, n). For the MPP, the shift towards low frequencies of the modes is due to the

(m, n)	$\eta_{mn}(\%)$	ΔY_{mn} (dB)
$(1, 1)$	1.06	38
$(1, 2)$	0.35	30
$(2, 1)$	0.25	27
$(2, 2)$	0.12	21

Table 1: Modal loss factor η_{mn} and mobility reduction ΔY_{mn} for mode (m, n) of a simply supported MPP whose mobility is indicated in Figure 2. Loss factor of aluminum is set to a constant value of $\eta_{\text{s}} = 0.01\%$.

reduction of the Young's modulus via C_ϕ in Equation (2). The perforations increase the loss factor and therefore the added damping relative to the reference plate by a factor of 106 in the first mode, 35 in the second mode, 25 in the third mode and 12 in the fourth mode.

In Figure 2, an additional comparison is made, where the MPP keeps the same specific stiffness as the reference plate. Here, the specific rigidity is the ratio between the rigidity and the surface mass $(D/\rho h)$. This comparison aims to confirm that the increase in damping is indeed due to the losses added by the perforations and not to the reduction in the rigidity of the plate.

3. MPP: Uniform distribution and multiple diameters

3.1. Homogenization model

In this section, an MPP with N groups of perforations is considered. All perforations in a same group have the same diameter d_k with $k = 1, 2, \cdots, N$. Each group of perforations is homogeneously distributed

over the MPP which can be considered homogeneous. To capture the dynamic response of an MPP with multi-size perforation diameters, a homogenization approach is proposed. The principle is to model the heterogeneous MPP structure as an equivalent continuous structure. In this context, $2N$ equivalent plates, defined in the same mathematical spatial domain, are considered: N equivalent homogeneous solid plates and N equivalent homogeneous fluid plates as shown in Figure 3 for an MPP with two groups of perforations. Each homogeneous solid plate is related to its perforations diameter d_k and its corresponding perforation ratio $\phi_k^{(0)}$[2]. The fluid flow in each subdomain is independent of the other subdomains (no direct

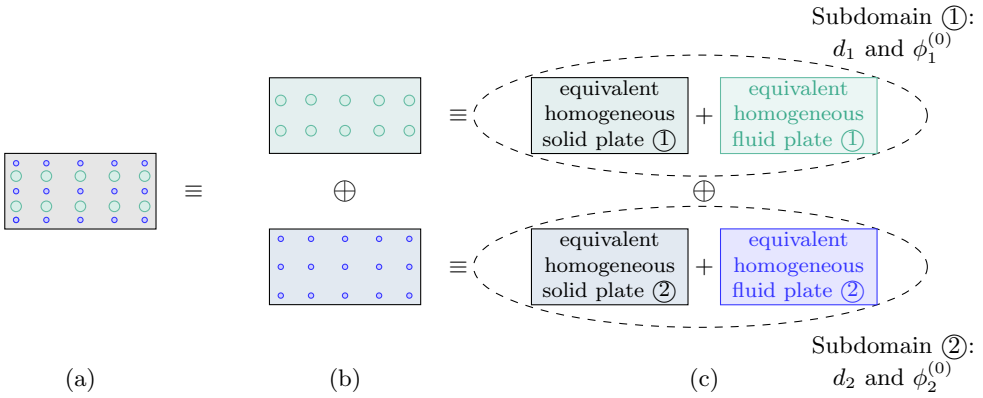

Figure 3: MPP with two groups of perforations with two perforation diameters d_1 and d_2. The MPP shown in (a) is decomposed into two equivalent MPP, each associated with a perforation diameter and ratio, as illustrated in (b). The two MPP in (b) are considered as the sum of two pairs of equivalent homogeneous plates shown in (c): an equivalent homogeneous fluid plate and an equivalent homogeneous solid plate. Each pair is related to the corresponding d_k and $\phi_k^{(0)}$ with $k = 1$ or 2.

coupling). The properties of each subdomain (perforation ratio, resistivity) are considered separately. A perforation ratio $\phi_k^{(0)}$ is associated with each perforation diameter d_k and the total perforation ratio is

$$\phi_{\text{tot}}^{(0)} = \sum_{k=1}^{N} \phi_k^{(0)}. \tag{8}$$

The overall airflow resistivity of the equivalent plate with N perforation diameters takes the form [15, 9, 31]

$$\frac{1}{\sigma} = \sum_{k=1}^{N} \frac{1}{\sigma_k^{(0)}} \tag{9}$$

where $\sigma_k^{(0)}$ is given by Equation (4) with $d = d_k$. If $\alpha_\infty \approx 1$, only the resistivity is modified by the addition of perforations of different sizes. For the considered $\phi_{\text{tot}}^{(0)}$, the tortuosity end correction has limited influence on the results. However, to account for the size of multiple perforations in the empirical formulation of the tortuosity of the length correction from [3] given in Equation (5), an average approach is proposed here. The tortuosity is thus rewritten

$$\alpha_\infty = 1 + B_{\text{tot}}(1 - 1.14\sqrt{\phi_{\text{tot}}^{(0)}}) \quad \text{with} \quad B_{\text{tot}} = \frac{1}{\phi_{\text{tot}}^{(0)}} \sum_{k=1}^{N} \phi_k^{(0)} B_k \tag{10}$$

where B_k defined in Equation (5) is applied to each subdomain k.

The bending stiffness is also modified in order to capture the effect of the multi-size microperforations in the dynamic response of the plate. To this end, the correction coefficient C_ϕ in Equation (2) becomes a function of $\phi_{\text{tot}}^{(0)}$. Equations (8) to (10) are then inserted in Equation (1) to obtain the structural response for an MPP with homogeneous distribution of multiple microperforations.

Multi-size microperforations are expected to increase the frequency range over which the added damping is effective. As said in Section 2.2, the added damping reaches a maximum at a characteristic frequency, that is only a function of the diameter of the perforation, as defined in Equation (6), and acts on a frequency range around f_c. Assuming that each added damping phenomenon is independent, the

[2]Note that the equivalent solid plate of subdomain k is defined by its perforation ratio $\phi_k^{(0)}$. The definition of the global equivalent solid plate is achieved by an electroacoustic analogy [20, 24]. According to this approach, Young's modulus and density of the overall structure are defined as a function of the overall perforation ratio given in Equation (8).

use of N groups of perforations of different diameters induces N characteristic frequencies of maximum damping on the same MPP and thus increases its efficiency. In Figure 4, we vary the thickness of the plate described in the previous section, in the range $h \in 0.5 - 3\,\text{mm}$, in order to vary the resonance frequency of its first two modes. Consequently, the loss factor η_i is obtained as a function of the resonance frequency f_i in Figure 4(a) for $i = 1$ and in Figure 4(b) for $i = 2$. Three configurations are considered in terms of d. In the first, the diameter of the perforation d_1 is chosen to induce a maximum added damping in the first natural mode. In the second, the diameter of the perforation d_2 is set to maximize the added damping in the second natural mode. In the third configuration, a combination of d_1 and d_2 is considered. The corresponding perforation ratios are $\phi_1^{(0)} = 3\,\%$ and $\phi_2^{(0)} = 7\,\%$. For each configuration, the overall perforation ratio, defined from Equation (8), is set to $10\,\%$[3]. For mode i with $i = 1, 2$, an MPP with two

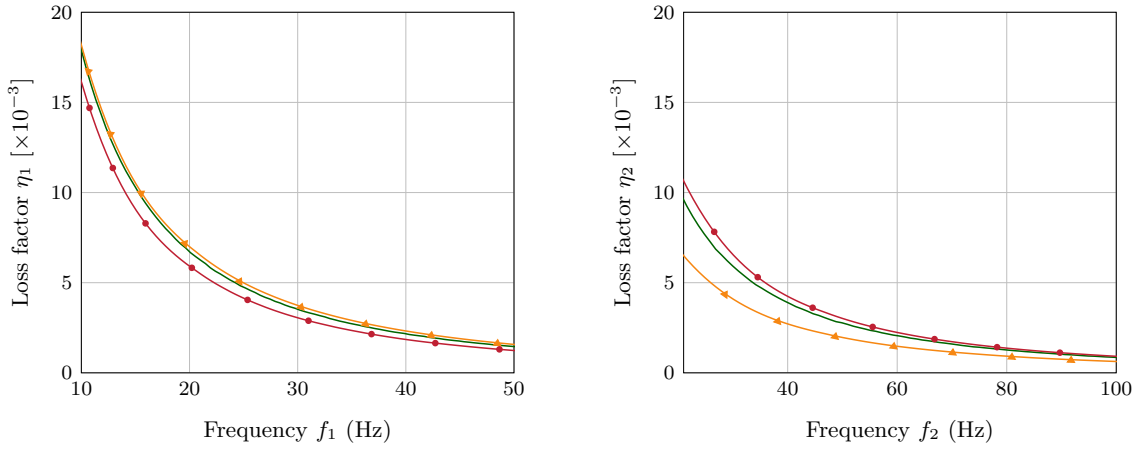

(a) (b)

Figure 4: Loss factor for two modes. (a) first mode. (b) second mode. (—▲—) d_1 set to maximize added damping on the first mode with $\phi^{(0)} = 10\,\%$; (—●—) d_2 set to maximize the added damping on the second mode with $\phi^{(0)} = 10\,\%$; (——) combination of d_1 and d_2 with associated perforation ratios $\phi_1^{(0)} = 3\,\%$ and $\phi_2^{(0)} = 7\,\%$ where the total perforation ratio, defined from Equation (8), is $\phi_{\text{tot}}^{(0)} = \phi_1^{(0)} + \phi_2^{(0)} = 10\,\%$.

groups of perforations provides similar results to the case of an MPP with a single group of perforations, where the diameter is chosen to maximize the added damping on the considered mode. The damping induced by the MPP with two groups of perforations on mode i is always higher than the one induced on mode k, $i \neq k$, by an MPP with a single group of perforations. As a consequence, a multi-size perforation MPP does not decrease (or slightly decreases) the added damping efficiency on mode i compared to an MPP where d is chosen to maximize damping on mode i only but allows for efficiency on multiple modes. The perforation ratio of each subdomain also influences the added damping. In fact, mode i is all the more damped as the perforation ratio of the subdomain k is large. It is therefore possible to adjust $\phi_k^{(0)}$ to maximize the added damping on a mode or to maximize the effect on the N modes.

In order to maximize the added damping in the frequency range between the natural frequencies p and q, the formula of the perforation diameter of each subdomain, denoted d_p and d_q respectively, is defined as follows

$$d_p = \sqrt{\frac{16\mu_{\text{f}}}{\pi f_p \rho_{\text{f}} \alpha_\infty}}, \tag{11}$$

where f_p is the natural frequency of the pth mode. A similar expression is given for d_q from f_q. The ω-dependent loss factors $\eta_p(\omega)$ and $\eta_q(\omega)$ can be calculated from Equation (48) of reference [13]. These loss factors respectively show maximum added damping $\eta_p^{\max}$ at f_p and $\eta_q^{\max}$ at f_q. If one defines the absolute difference $|\eta_p(\omega) - \eta_p^{\max}|/\eta_p^{\max} - |\eta_q(\omega) - \eta_q^{\max}|/\eta_q^{\max}|$, it can be shown that an overall maximum added damping occurs at the geometric mean of f_p and f_q given by

$$f_{\text{c}} = \sqrt{f_p f_q}. \tag{12}$$

[3]As the model is a homogenized one, perforations are not considered in a discreet way. In practice, if the perforation ratios of each subdomain are too important, there is a risk of overlapping perforations. Furthermore, in order to preserve the mechanical properties of the structure (equivalent Young's modulus and equivalent density) which are influenced by ϕ , the total perforation ratios studied in this paper are less than 25 %.

This overall maximum damping would typically be obtained when

$$\phi_p^{(0)} = \frac{\phi_{\text{tot}}^{(0)}}{1 + \frac{f_q}{f_p}} \text{ and } \phi_q^{(0)} = \frac{\phi_{\text{tot}}^{(0)}}{1 + \frac{f_p}{f_q}}. \tag{13}$$

Using the latter equations, with $\phi_{\text{tot}} = 10\,\%$ and the graphs in Figure 4, one obtains $\phi_p^{(0)} \approx 3\,\%$ and $\phi_q^{(0)} \approx 7\,\%$. This gives the green curves in Figure 4 for the combination of the two sets of perforations. These curves nearly reach the maximum loss curves for the single-perforation configuration for both modes.

3.2. Experimental validation

In this section, the experimental validation of the previous approach is performed. The experimental setup presented is used in Sections 4 and 5. The mechanical parameters of the MPP such as Young's modulus and structural loss factor are determined from the Oberst test bench developed by Mecanum Inc. and presented in Figure 5(a). The measuring method follows the ASTM E756-05(2017) [12] standard. The tested sample is clamped at $x = 0$ and free at $x = L_x$. It is excited by an external force of amplitude F_{ext} at $(x_F, y_F) = (L_x, L_y/2)$ and the sample vibratory response is measured by a magnetic sensor located at point $(x_R, y_R) = (R, L_y/2)$.

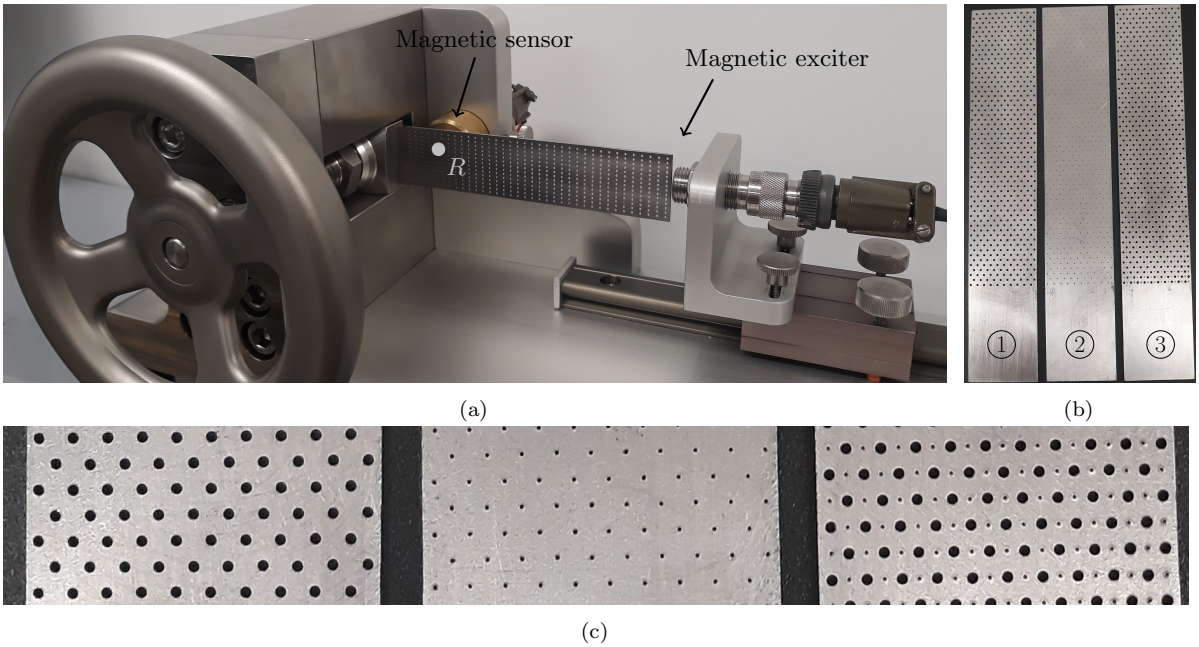

(a) (b)

(c)

Figure 5: Test bench in (a) and MPP sample in (b) used in the experimental validation of the model presented in Section 3.1. The zoom (c) corresponds to a focus on the perforations of (b).

In order to validate the homogenized model of the multi-size MPP, the three samples presented in Figure 5(b) are considered and noted MPP①, MPP② and MPP③. They are made of steel and have a length $L_x = 130\,\text{mm}$, a width $L_y = 30\,\text{mm}$, and a thickness $h = 0.87\,\text{mm}$. For MPP①, $d \equiv d_1$ is set to induce the maximum added damping around the first natural frequency f_1. For MPP②, $d \equiv d_2$ is chosen to maximize the added damping around the second natural frequency f_2. The perforation ratios associated with diameters d_1 and d_2 are $\phi_1^{(0)} = 10\,\%$ and $\phi_2^{(0)} = 2.3\,\%$ respectively. MPP③ is a combination of MPP① and MPP②. The resulting MPP therefore has two groups of perforation with the two perforation diameters d_1 and d_2 with corresponding perforation ratios $\phi_1^{(0)}$ and $\phi_2^{(0)}$. Moreover, MPP① and MPP② have an equal number of perforations but $d_1 > d_2$ and thus $\phi_1^{(0)} > \phi_2^{(0)}$. MPP③ has therefore the double number of perforations compared to MPP① and MPP②. The perforation parameters of each MPP are listed in Table 2.

Plate mobility levels, as defined in the previous section, are plotted for the three MPP in Figure 6. The figure compares the experimental measurements made on MPP①, MPP②, and MPP③. It also compares the analytical prediction made on MPP③. As expected, the levels of mobility at the first resonance are similar for MPP① and MPP③. However, compared to MPP①, a reduction of about 3.8 dB is observed on the second resonance for the multiple perforations MPP③. It can also be noticed that the analytical model gives similar results as the experiments and which validates the model presented in Section 3.1.

	$\phi_1^{(0)}$ (%)	d_1 (mm)	$\phi_2^{(0)}$ (%)	d_2 (mm)	$\phi_{\text{tot}}^{(0)} = \phi_1^{(0)} + \phi_2^{(0)}$ (%) (8)
MPP①	10	1	·	·	10
MPP②	·	·	2.3	0.5	2.3
MPP③	10	1	2.3	0.5	12.3

Table 2: Measured sample perforation parameters.

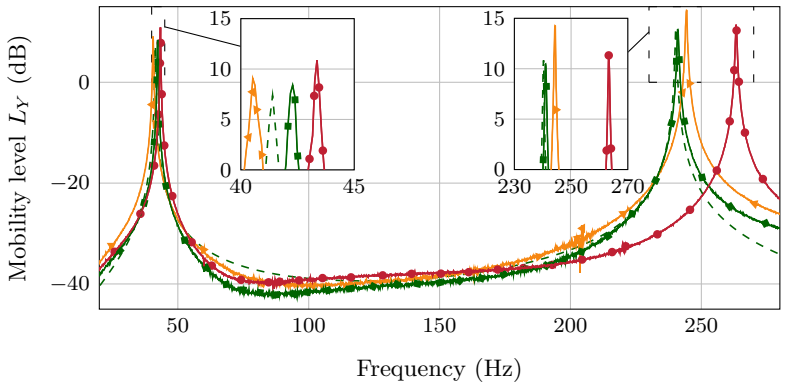

Figure 6: Mobilities for: (—▲—) measured MPP① which acts as the reference MPP; (—●—) measured MPP②; (—■—) measured MPP③; (- - -) analytical MPP③. Perforation parameters for MPP① and MPP③ are given in Table 2.

From the plate mobility levels shown in Figure 6, the loss factors are measured using the half-power bandwidth method at the first two resonances for the three MPP. The measured loss factors are summarized in Table 3. For MPP③, the loss factor obtained from the theoretical homogenization model presented in Section 3.1 is also provided. It can be seen that for MPP③, the global damping is maximized at both resonances, unlike an MPP with single-size perforations, where the damping is only maximized locally on one mode.

	Mode 1		Mode 2	
	f_1 (Hz)	$\eta_1[\times 10^{-3}]$	f_2 (Hz)	$\eta_2[\times 10^{-3}]$
Measured MPP①	44.2 ± 2.1	0.65 ± 0.002	250.7 ± 3.6	0.14 ± 0.005
Measured MPP②	43.8 ± 0.3	0.34 ± 0.11	260.4 ± 1.9	0.24 ± 0.02
Measured MPP③	43.2 ± 0.5	0.75 ± 0.08	244.2 ± 1.7	0.23 ± 0.002
Analytical MPP③	41.4	0.81	240.3	0.20

Table 3: Values of experimental and theoretical loss factor with standard deviation for the three MPP presented in Figure 9(a). Each loss factor is determined for the ith mode. Perforation parameters are given in Table 2 for each MPP configurations.

The previous results show that using an MPP with a multi-size perforations increases the frequency band over which the added damping is effective. Moreover, it also increases the damping factor of the first modes. Finally, the comparison between the measured and analytical results obtained for MPP③ in Figure 6 and Table 3 allows one to validate the model proposed in Section 3.1.

4. MPP: Nonuniform distribution and single diameter

4.1. Perforation ratio gradient

The distribution of the perforations can also influence the added damping. For a given mode, the closer the perforations are to the maximum displacement zones, the higher the added damping. In fact, the damping added by the microperforations is due to the viscous friction in the boundary layers of the MPP. This viscous friction is all the more important as the relative velocity between the fluid and the structure is large. To enhance the added damping effect, it is therefore possible to concentrate the perforations on the antinodes of the modes whose amplitude must be reduced. In this section, only a single perforation diameter is considered, and the perforation ratio is written in terms of a distribution function to explore this effect:

$$\phi(x, y) = \phi^{(0)}\, \text{Ih}(x, y) \tag{14}$$

where $\mathbb{Ih}(x,y)$ is a normalized inhomogeneity function and $\phi^{(0)}$ the maximum value of the perforation ratio obtained at $\max \mathbb{Ih}(x,y) = 1$. The perforation ratio in the previous equation is a local variable. Its integration over the whole plate surface yields the global perforation ratio

$$\phi_{\mathrm{g}} = \frac{\phi^{(0)}}{L_x L_y} \int_0^{L_x} \int_0^{L_y} \mathbb{Ih}(x,y) \mathrm{d}y \mathrm{d}x. \tag{15}$$

In Equation (3), D and α_∞ depend on the perforation ratio and become a spatial function by considering the perforation ratio gradient defined in Equation (14). The correction function in the bending stiffness of Equation (2) is rewritten as

$$C_\phi(x,y) = \frac{(1-\phi(x,y))^2}{1+(2-3\nu)\phi(x,y)}. \tag{16}$$

Similarly, the corrected tortuosity given by Equation (5) now rewrites $\alpha_\infty(x,y) = 1 + B - 1.14B\sqrt{\phi(x,y)}$. Note that the perforation ratio also has an influence on ν [2]. However, for the perforation ratios considered, ν is assumed to be constant [17, 2]. Equations (14) and (16) are inserted into Equation (3) to capture the effect of the perforation ratio gradient in the structural dynamics of MPP. The system of equations describing the autonomous response of a finite MPP saturated by a lightweight fluid in its perforations then becomes

$$h(\rho_{\mathrm{s}}(1-\phi(x,y))\ddot{w}_{\mathrm{s}} + \rho_{\mathrm{f}}\phi(x,y)\ddot{w}_{\mathrm{f}}) + D(x,y)\nabla^4 w_{\mathrm{s}} = 0, \tag{17a}$$

$$\rho_{\mathrm{f}}((1-\alpha_\infty(x,y))\ddot{w}_{\mathrm{s}} + \alpha_\infty(x,y)\ddot{w}_{\mathrm{f}}) + \varsigma(\dot{w}_{\mathrm{f}} - \dot{w}_{\mathrm{s}}) + K_{\mathrm{f}}\nabla^2 w_{\mathrm{s}} = 0. \tag{17b}$$

Classical modal analysis is now performed in the same vein as in [13]. The equations must be space semi-discretized and projected onto the non-perforated plate mode. The plate displacement is assumed to be of the form

$$w_{\mathrm{s}}(x,y,t) = \sum_{m=1}^{\infty}\sum_{n=1}^{\infty} w_{mn}^{\mathrm{s}}(t)\Psi_{mn}(x,y), \tag{18}$$

where $w_{mn}^{\mathrm{s}}(t)$ represent the participation of non-perforated plate eigenmode $\Psi_{mn}(x,y)$ determined from boundary conditions. A similar expression holds for the fluid. Equation (18) is rewritten for a finite number of modes and rearranged in lexicographic order according to i. Each pair $(m,n) \in \mathbb{N}\times\mathbb{N}$ corresponds to a single index $i \in \mathbb{N}$. Equation (18) is therefore rewritten in terms of i such that

$$w_{\mathrm{s}}(x,y,t) = \sum_{i=1}^{N_{\mathrm{dof}}} w_i^{\mathrm{s}}(t)\Psi_i(x,y) \tag{19}$$

where N_{dof} is the number of degrees-of-freedom (dof) in plate discretization. The corresponding vector $\boldsymbol{\Psi}(x,y)$ is of size $N_{\mathrm{dof}} \times 1$ and stores the terms $\Psi_i(x,y)$. After this reorganization, Equation (17) are discretized and projected onto the plate and fluid eigenmode basis. To this end, the terms in Equation (17) are multiplied by $\boldsymbol{\Psi}^\top(x,y)$ and integrated on the plate surface S. The resulting system is written in the matrix form

$$\dot{\mathbf{z}}(t) = \mathbf{D}\mathbf{z}(t), \quad \text{where} \quad \mathbf{D} = \begin{bmatrix} \mathbf{0} & \mathbf{Id} \\ -\mathbf{M}^{-1}\mathbf{K} & -\mathbf{M}^{-1}\mathbf{C} \end{bmatrix}, \quad \mathbf{z}(t) = \begin{pmatrix} \mathbf{x}(t) \\ \dot{\mathbf{x}}(t) \end{pmatrix} \tag{20}$$

where $\mathbf{Id}$ is the identity matrix of rank $N_{\mathrm{dof}}/2$ and

$$\mathbf{x}(t) = \begin{pmatrix} \mathbf{w}_{\mathrm{s}}(t) \\ \mathbf{w}_{\mathrm{f}}(t) \end{pmatrix}; \quad \mathbf{M} = \begin{bmatrix} \mathbf{M}_{\mathrm{s}_1} & \mathbf{M}_{\mathrm{f}_1} \\ \mathbf{M}_{\mathrm{s}_2} & \mathbf{M}_{\mathrm{f}_2} \end{bmatrix}; \quad \mathbf{C} = \begin{bmatrix} \mathbf{0} & \mathbf{0} \\ \mathbf{C}_{\mathrm{s}_2} & \mathbf{C}_{\mathrm{f}_2} \end{bmatrix}; \quad \mathbf{K} = \begin{bmatrix} \mathbf{K}_{\mathrm{s}_1} & \mathbf{0} \\ \mathbf{K}_{\mathrm{s}_2} & \mathbf{0} \end{bmatrix}. \tag{21}$$

The displacement contributions of the solid are stored in $\mathbf{w}_{\mathrm{s}}$ and those of the fluid, in $\mathbf{w}_{\mathrm{f}}$. Each matrix of Equation (21) is written as follows:

$$\begin{aligned}
\mathbf{M}_{\mathrm{s}_1} &= h\rho_{\mathrm{s}} \iint_S (1-\phi(x,y))\boldsymbol{\Psi}\boldsymbol{\Psi}^\top \mathrm{d}x\mathrm{d}y, & \mathbf{M}_{\mathrm{s}_2} &= \rho_{\mathrm{f}} \iint_S (1-\alpha_\infty(x,y))\boldsymbol{\Psi}\boldsymbol{\Psi}^\top \mathrm{d}x\mathrm{d}y, \\
\mathbf{M}_{\mathrm{f}_1} &= h\rho_{\mathrm{f}} \iint_S \phi(x,y)\boldsymbol{\Psi}\boldsymbol{\Psi}^\top \mathrm{d}x\mathrm{d}y, & \mathbf{M}_{\mathrm{f}_2} &= \rho_{\mathrm{f}} \iint_S \alpha_\infty(x,y)\boldsymbol{\Psi}\boldsymbol{\Psi}^\top \mathrm{d}x\mathrm{d}y, \\
\mathbf{C}_{\mathrm{s}_2} &= -\varsigma \iint_S \boldsymbol{\Psi}\boldsymbol{\Psi}^\top \mathrm{d}x\mathrm{d}y, & \mathbf{C}_{\mathrm{f}_2} &= \varsigma \iint_S \boldsymbol{\Psi}\boldsymbol{\Psi}^\top \mathrm{d}x\mathrm{d}y, \\
\mathbf{K}_{\mathrm{s}_1} &= \iint_S D(x,y)\nabla^2\boldsymbol{\Psi}\nabla^2\boldsymbol{\Psi}^\top \mathrm{d}x\mathrm{d},y & \mathbf{K}_{\mathrm{s}_2} &= K_{\mathrm{f}} \iint_S \nabla^2\boldsymbol{\Psi}\boldsymbol{\Psi}^\top \mathrm{d}x\mathrm{d}y.
\end{aligned} \tag{22}$$

An analytical solution of the equation of motion is possible in the state space. Solutions for the ith mode take the form of eigenvalues $\lambda_i = \beta_i \pm j\gamma_i$ where $\beta_i = -\zeta_i/\omega_i$ is the damping term involved into the exponential decrease of the mode due to viscous friction and ζ_i is the modal damping ratio. The imaginary part $\gamma_i = \omega_i\sqrt{1-\zeta_i^2}$ corresponds to the natural frequency, where ω_i is the undamped angular frequency. The loss factor is related to ζ_i by $\eta_i = 2\zeta_i$.

In order to explore the influence of the spatial distribution of the perforation on the added damping[4], the loss factor of the first mode η_1 is plotted as a function of the global perforation ratio in Figure 7. In this figure, three spatial distributions are considered. The first configuration consists in perforations homogeneously distributed on the MPP. It corresponds to the reference MPP, i.e. $\mathbb{h}(x,y) = 1$. In the second configuration, the perforations are distributed according to the shape of the first plate mode without perforation thus $\mathbb{h}(x,y) = \sin(\pi x/L_x)\sin(\pi y/L_y)$. The normalized inhomogeneity function is equal to 1 at the maximum plate deflection. The spatial perforation ratio is defined via Equation (14). Finally, the third configuration consists in perforations distributed according to the step function

$$\mathbb{h}(x,y) = \Pi(x,y) = \begin{cases} 1 & \text{if} \quad \frac{1}{4} \leq \frac{x}{L_x} \leq \frac{3}{4} \quad \text{and} \quad \frac{1}{4} \leq \frac{y}{L_y} \leq \frac{3}{4}, \\ 0 & \text{else.} \end{cases} \tag{23}$$

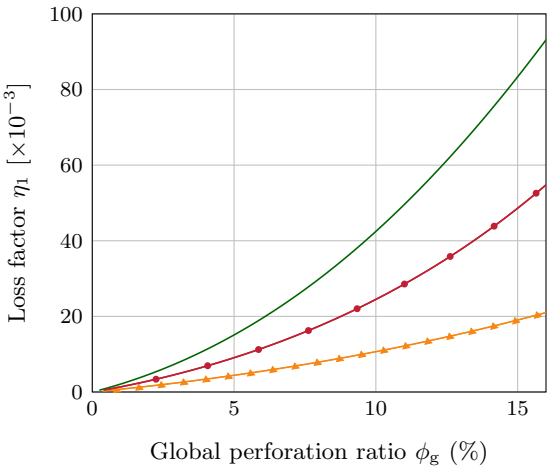

Figure 7: Loss factor for the first mode of a 570 mm × 490 mm × 1 mm simply-supported aluminum MPP with $d = 1.4$ mm: (—▲—) uniform distribution with $\mathbb{h}(x,y) = 1$; (—●—) distribution along plate mode shape according x with $\mathbb{h}(x,y) = \sin(\pi x/L_x)\sin(\pi y/L_y)$; (——) distribution according to the rectangular function $\mathbb{h}(x,y) = \Pi(x,y)$ defined in Equation (23).

As mentioned previously, the additional damping exhibited by MPP is closely related to the viscous friction in the boundary layers of MPP, which is more important the higher the relative velocity between the fluid and the structure. In fact, fluid viscosity leads to drag forces at the fluid-solid interface in the perforation, resulting in dissipation mechanisms affecting the dynamic response of both fluid and solid. The viscous force per unit volume is defined by [4, 5] as a function of ω proportional to σ and the relative fluid-solid velocity. Adapted for an MPP with inhomogeneous spatial distribution of perforation under low frequency assumptions, the viscous friction force can be recast as

$$f_\mathrm{v}(x,y,t) = \frac{32\mu_\mathrm{f}\phi(x,y)}{d^2}(\dot{w}_\mathrm{f}(x,y,t) - \dot{w}_\mathrm{s}(x,y,t)). \tag{24}$$

The larger the velocity difference, the greater the friction force. The dissipative effects are directly proportional to the viscous force, generated by friction taking place in the thermo-viscous skin at the level of the solid wall of the perforations, and are captured in Equations (1), (3) and (17) by the velocity term which corresponds to $f_\mathrm{v}(x,y,t)$. From the discretization in Equation (19), Equation (24) reads

$$f_\mathrm{v}(x,y,t) = \frac{32\mu_\mathrm{f}\phi(x,y)}{d^2}\sum_i^{N_\mathrm{dof}} \Psi_i(x,y)(\dot{w}_i^\mathrm{f}(t) - \dot{w}_i^\mathrm{s}(t)). \tag{25}$$

[4]Due to the distribution of perforations along the deformations of the first resonance mode, i.e. $i = 1$, only the added damping presented by the first mode is taken into account in this section. The same considerations can be made for another mode, i.e. $i > 1$.

For a given mode, maximizing $\Psi_i(x, y)$ leads to maximizing the friction force and thus the additional damping of the MPP. Values of x and y for which $\Psi_i(x, y)$ reaches a maximum can be obtained depend on the size of the plate and on the boundary conditions involved in defining the eigenfunction. For a given d, the viscous force and, thus, the additional damping induced by the microperforations, is maximal for the ith mode when $x = x_{\max}$ is the solution of $\partial_x \Psi_i(x, y) = 0$ and when $y = y_{\max}$ is the solution of $\partial_y \Psi_i(x, y) = 0$. The added damping increases with the perforation ratio. It is therefore possible to increase the added damping by increasing the perforation ratio around the point $(x_{\max}, y_{\max})$. However, the concentration of perforations on the zones of interest, i.e. presenting maximum deflection amplitudes, will have a lower mechanical resistance, due to the modification of the Young's modulus. In addition, the more abrupt the change, the greater the stress concentrations at the point of failure, which reduces the mechanical strength of the structure.

Moreover, the spatial distribution of the perforation has an influence on the Young modulus of the structural part and thus on the MPP stiffness. For the first MPP mode of the three MPP represented in Figure 7, the MPP stiffness K_{s1}^{11}, where exponent 11 corresponds to the term's position in the stiffness matrix, given in Equation (22), is plotted versus ϕ_{g} in Figure 8. For the same ϕ_{g}, the plate stiffness decreases significantly when the concentration of perforations is shifted to the maximum deflection area of the plate.

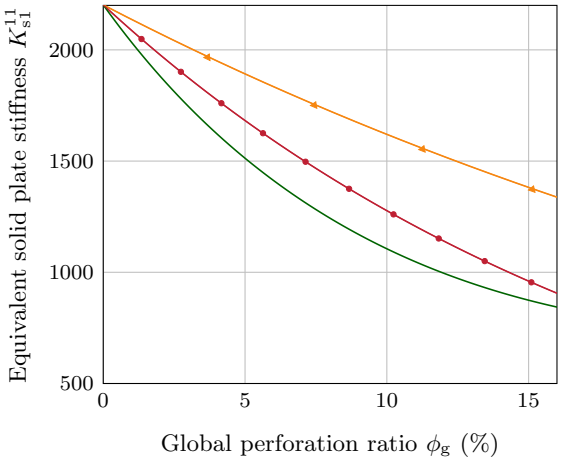

Figure 8: Equivalent solid plate stiffness K_{s1}^{11} for the first mode of a 570 mm × 490 mm × 1 mm simply-supported aluminum MPP with $d = 1.4$ mm as a function of the global perforation ratio ϕ_{g} for three different spatial perforation distributions: (—▲—) uniform distribution with $\mathbb{h}(x, y) = 1$; (—●—) distribution along plate mode shape according x with $\mathbb{h}(x, y) = \sin(\pi x/L_x)\sin(\pi y/L_y)$; (——) distribution according to the rectangular function $\mathbb{h}(x, y) = \Pi(x, y)$ defined in Equation (23).

4.2. Experimental validation

In this section, the experimental validation is performed on the Oberst test bench detailed in Section 3.2. The tested MPP samples are presented in Figure 9(a) and measure 131 mm × 30.7 mm × 1.08 mm. The overall perforation ratio and the diameter of the perforations are constant for the three plates and fixed at $\phi_{\mathrm{g}} = 10\,\%$ and $d = 1$ mm, respectively. For MPP④ the perforations are homogeneously distributed over the structure. In this validation section, MPP④ acts as the reference MPP. For MPP⑤, the perforation ratio is chosen as a linear function of x with a maximum at $x = L_x$ (maximum plate deflection for the first mode) such that $\phi(x) = \phi^{(0)} x/L_x$ with $\phi^{(0)} = 20\,\%$. For MPP⑥, the perforation ratio is defined by

$$\phi(x) = \phi^{(0)}\Pi(x) \quad \text{with} \quad \Pi(x) \begin{cases} 1 & \text{if } \frac{x}{L_x} \geq \frac{1}{2}, \\ 0 & \text{else.} \end{cases} \tag{26}$$

where $\phi^{(0)} = 20\,\%$. All perforation parameters and $\mathbb{h}(x)$ homogeneity functions for the three MPP of Figure 9(a) previously presented are reported in Figure 9(b). The experimental results are presented in Figure 10 and Table 4.

In Figure 10, the plate mobilities for the first mode of MPP⑤ and MPP⑥ are compared to those obtained for the reference MPP④ and non-perforated plate. On the one hand, an amplitude reduction of about 8 dB is observed with MPP⑤ and MPP⑥ compared to the case of the non-perforated plate. On the other hand, the amplitude reduction between MPP with spatial distribution (MPP⑤ and MPP⑥) and the reference MPP④ is about 3 dB. The resonance frequency is shifted due to the reduction in stiffness, which is successively higher for MPP⑥, MPP⑤ and MPP④. Finally, the good comparisons between

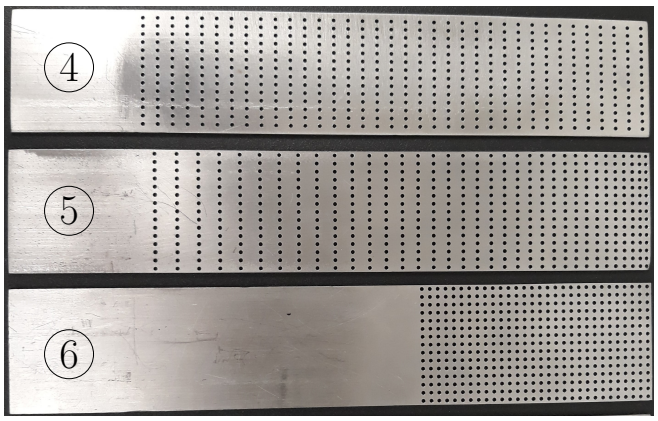

(a)

	$\phi^{(0)}$ (%)(15)	$\mathbb{h}(x)$ (%)
MPP④	10	1
MPP⑤	20	$\frac{x}{L_x}$
MPP⑥	20	$\Pi(x)$ defined in Equation (26)

(b)

Figure 9: Tested MPP samples with various space-dependent distributions of the perforation ratio. (a) — MPP④ homogeneous distribution: reference MPP, MPP⑤ linear distribution, MPP⑥ concentrated distribution located at the maximum of the deflection amplitude. (b) — Perforation parameters and homogeneity function $\mathbb{h}(x)$ for the three MPP presented in Figure 9(a). Perforation diameter is set to $d = 1\,\text{mm}$ in order to induce maximum damping around the first mode (i.e. $i = 1$) and global perforation ratio $\phi_\text{g} = 10\,\%$ identical for all three MPP.

the measurements and theoretical predictions shown in Figure 10, for MPP⑤ and MPP⑥, validate the analytical model presented in Section 4.1.

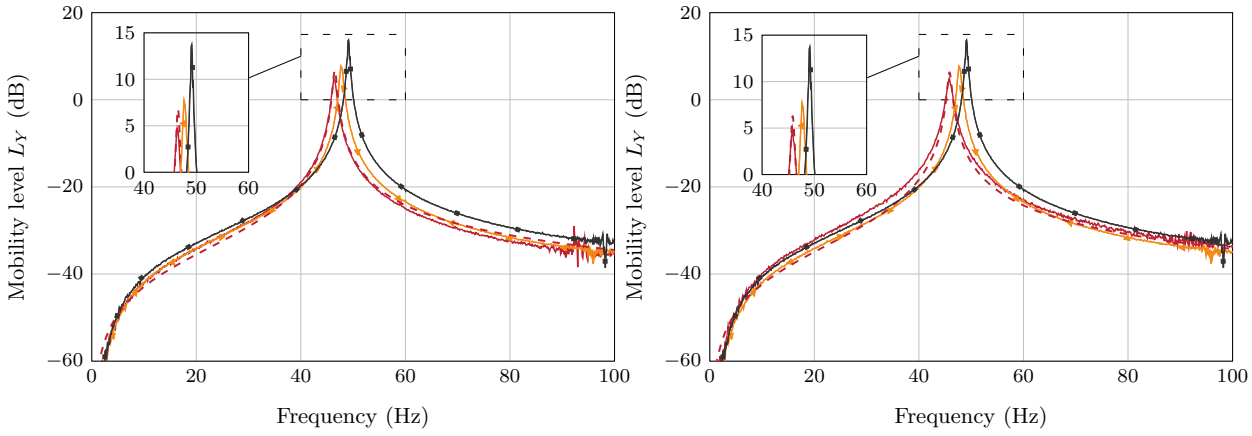

(a) (b)

Figure 10: Theoretical and experimental mobilities around mode 1 of (a) MPP⑤ and (b) MPP⑥. Comparisons between (——) measured and (- - -) theoretical. In (a) and (b), the measured mobilities of the reference MPP④ (—▲—) and non-perforated plate (—■—) are also provided. MPP perforation parameters are given in Figure 9(b).

From the mobilities measured, the loss factor is calculated at the first mode $i = 1$. The results are given in Table 4 for the studied MPP and reference non-perforated plate. In addition, the analytical model of Section 4.1 was also considered for calculating the loss factor of the first mode for the three MPP. One can observe that the analytical values agree well with the measurements. Also, for the same overall perforation ratio, distributing the perforations over the maximum deflection areas of the MPP increases the added damping by 62 % over the reference MPP④ and 133 % over the non-perforated plate.

To conclude this section, we have used an MPP whose microperforations are distributed along the vibrational antinodes of the modes we wish to damp. The proposed analytical model is validated by experimental measurements and shows that an MPP with distributed perforations maximizes the added damping compared to a uniform MPP. This is because the added damping is linked to the dissipation induced in the boundary layers that support the motion. The greater the deflection of the plate, the more

	Measured		Analytical	
	f_1 (Hz)	$\eta_1[\times 10^{-3}]$	f_1 (Hz)	$\eta_1[\times 10^{-3}]$
Reference non-perforated plate ①	47.9 ± 0.36	0.9 ± 0.073	·	·
MPP④	48.1 ± 0.12	1.3 ± 0.075	47.2	1.2
MPP⑤	48.4 ± 0.50	1.7 ± 0.190	46.5	1.6
MPP⑥	48.0 ± 1.97	2.1 ± 0.079	45.8	2.0

Table 4: Measured with standard deviation and analytical frequencies of the first mode plate and corresponding loss factors for the reference non-perforated plate ① and the three MPP presented in Figure 9(a) and perforation parameters are given in Table 2. Theoretical results obtained though the model proposed in Section 4.1 provided for $i = 1$.

viscous friction is present, thus increasing damping. To achieve damping in a given mode, it is therefore advisable to distribute the perforations over its vibratory antinodes. However, a large concentration of perforations in a small area can generate a stress concentration that could reduce the mechanical strength of the structure. This aspect must be carefully considered when designing the MPP.

5. MPP: Nonuniform distribution and multiple diameters

The aim of this section is to combine the two effects presented in Sections 3 and 4. Recall that Section 3 proposes to increase the frequency range of effective damping by employing multiple perforation diameters, and Section 4 suggests increasing the maximum added damping by using a perforation distribution according to modal deflections. It is therefore proposed to explore the damping capabilities of the MPP with a spatial distribution of multi-sized perforations. The idea is to design an MPP that improves the frequency range of the effective damping while maximizing the added damping on the frequencies of interest, i.e. the resonance frequencies of the structure.

Here, both analytical models exposed in Sections 3 and 4 are combined to obtain the dynamic response of an MPP involving space-dependent distributions of multi-size perforations. The MPP is assumed to be equivalent to N independent MPP, each with its own perforation diameter d_k, perforation ratio $\phi_k^{(0)}$, and inhomogeneity function Π_k, $k = 1, 2, \ldots, N$. Based on a homogenization model similar to the one presented in Section 3, the equations of motion generalize to (time and space dependencies are dropped out for the purpose of readability)

$$h(\rho_s(1-\phi(x,y))\ddot{w}_s + \rho_f\phi(x,y)\ddot{w}_f) + D(x,y)\nabla^4 w_s = 0 \tag{27a}$$

$$\rho_f((1-\alpha_\infty(x,y))\ddot{w}_s + \alpha_\infty(x,y)\ddot{w}_f) + \sigma(x,y)\phi(x,y)(\dot{w}_f - \dot{w}_s) + K_f\nabla^2 w_s = 0 \tag{27b}$$

with

$$\frac{1}{\sigma(x,y)} = \sum_{k=1}^{N} \frac{1}{\sigma_k(x,y)}. \tag{28}$$

The spatial bending coefficient $D(x,y)$ is expressed in terms of the global spatial perforation ratio $\phi(x,y)$ defined through Equation (8) applied to $\phi_k(x,y)$. The global spatial resistivity $\sigma(x,y)$ is defined from the resistivity of each equivalent plate derived from d_k and $\phi_k(x,y)$. The global spatial tortuosity is also expressed using Equation (10) applied to the spatial perforation ratio $\phi_k(x,k)$ and the perforation diameter of the subdomain k.

The validation of the generalized model in Equation (27) is now exposed. To this aim, two plates of dimension 195 mm × 30.7 mm × 1.17 mm are considered: a non-perforated reference plate ② and MPP⑦ with multiple perforation diameters spatially distributed along a non-homogeneous pattern. To maximize the damping added by the microperforations on modes 1 and 2, two diameters of perforations are chosen: $d_1 = 1.3$ mm and $d_2 = 0.7$ mm, corresponding to characteristic frequencies $f_{c_1} \approx 27$ Hz and $f_{c_2} \approx 114$ Hz, respectively. MPP⑦ which is presented in Figure 11 is decomposed into three equivalent plates with respective perforation ratios and inhomogeneity functions defined as:

$$\phi_1(x) = \phi_1^{(0)}\Pi_1(x) \quad \text{with} \quad \Pi_1(x) = \begin{cases} 1 & \text{if } \frac{x}{L_x} \geq 0.695, \\ 0 & \text{otherwise} \end{cases} \quad \text{and} \quad \phi_1^{(0)} = 33\,\%, \tag{29a}$$

$$\phi_2(x) = \phi_2^{(0)}\Pi_2(x) \quad \text{with} \quad \Pi_2(x) = \begin{cases} 1 & \text{if } \frac{x}{L_x} \geq 0.8, \\ 0 & \text{otherwise} \end{cases} \quad \text{and} \quad \phi_2^{(0)} = 11\,\%, \tag{29b}$$

$$\phi_3(x) = \phi_3^{(0)}\Pi_3(x) \quad \text{with} \quad \Pi_3(x) = \begin{cases} 1 & \text{if } 0.165 \leq \frac{x}{L_x} \leq 0.695, \\ 0 & \text{otherwise} \end{cases} \quad \text{and} \quad \phi_3^{(0)} = 16\,\%. \tag{29c}$$

The ratio $\phi_1(x)$ is associated with perforations of diameter, d_1 while $\phi_2(x)$ and $\phi_3(x)$ are related to perforations of diameter d_2.

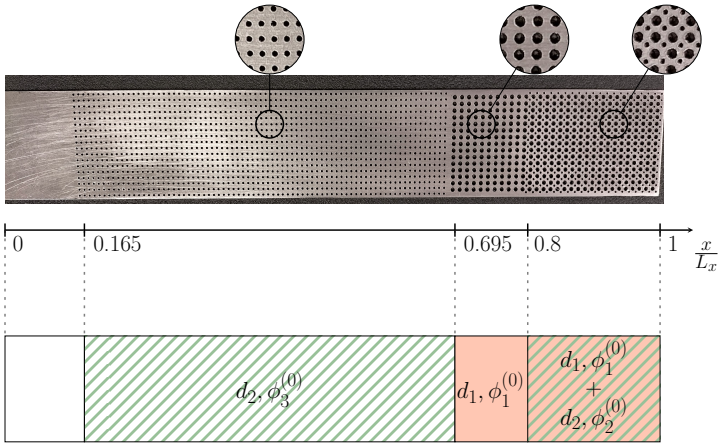

Figure 11: MPP⑦: spacial perforation distribution described in Equation (29).

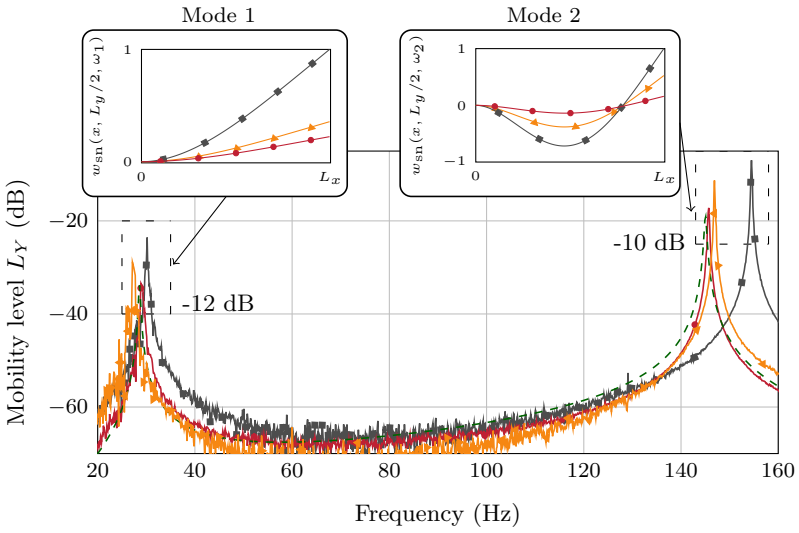

Figure 12: Plate mobility in dB with: (—●—) measured MPP⑦ shown in Figure 11, (—■—) measured reference non-perforated plate ②, (—▲—) measured reference MPP with $d = d_1$ and (- - -) theoretical MPP⑦. MPP⑦ is considered as three equivalent MPP inhomogeneous spacial distribution of perforations defined in Equation (29). Spacial distribution (29a) associated with $d_1 = 1.3\,\text{mm}$ while spacial distributions (29b) and (29c) are related to $d_2 = 0.7\,\text{mm}$. Loss factor and Young's modulus used in the theoretical model are obtained experimentally from measurements on the non-perforated plate. The corresponding analytical modal displacement $w_{sn}(x, L_y/2, \omega_i)$ given in Equation (30) are also presented for: (—●—) analytical MPP ⑦, (—■—) analytical reference non-perforated plate ②, (—▲—) analytical reference MPP.

The test bench described in Section 3.2 is used to obtain the MPP mobility. In Figure 12, the mobility measured for MPP⑦ is compared to that of the non-perforated reference plate ② and the analytical mobility calculated for the MPP. The shapes of the corresponding normalized analytical modal displacement

$$w_{sn}(x, L_y/2, \omega_i) = \frac{w_s(x, L_y/2, \omega_i)}{\max(w_{s,ref}(x, L_y/2, \omega_i))}, \tag{30}$$

are also presented, where $\max(w_{s,ref}(x, L_y/2, \omega_i))$ is the maximum of deflection obtained for the reference non-perforated plate.

Table 5 summarizes the main comparison data. On the one hand, the measured results show a magnitude reduction of approximately 12 dB for the first resonance frequency, while the magnitude reduction is approximately 10 dB for the second resonance frequency. On the other hand, the loss factor is nearly doubled at both resonances in the case of MPP⑦ compared to the case of the non-perforated plate. Finally, the predicted theoretical results for MPP⑦ are in close agreement with the measurements for

	Mode 1		Mode 2	
	f_1 (Hz)	$\eta_1[\times 10^{-3}]$	f_2 (Hz)	$\eta_2[\times 10^{-3}]$
Measured reference non-perforated plate ②	33.41	0.63	147.7	0.15
Measured MPP⑦	31.41	1.26	142.4	0.29
Analytical MPP⑦	28.6	1.25	145.1	0.25

Table 5: Values of experimental and theoretical loss factor for the MPP⑦ presented in Figure 11. Each loss factor is determined for the ith mode. Perforation are described in Equation (29).

MPP⑦. The shape of the modal displacement presented in Figure 12 shows that perforations substantially reduce the amplitude of displacement of the structure. Moreover, using a double set of perforations distributed over the antinodes of the modes maximizes this added damping effect. A comparison between the non-perforated reference plate and the two MPPs shows that the presence of perforations has little influence on the shape of the structure's displacements. These results seem to show that the implementation of multi-size microperforations combined with inhomogeneous spatial distributions of perforations has two advantages: (1) depending on the diameters chosen, the added damping is effective over a wider frequency band compared to a plate with a single set of perforations; (2) the well-chosen distribution of the perforations over certain areas of interest also maximizes the added damping.

6. Conclusion

This article extends the theoretical model developed in [13] to study the added damping effect exhibited by microperforated plates (MPP) embedding: (i) multi-size perforation diameters; (ii) spatial distributions of perforation, and (iii) a combination of (i) and (ii). For this purpose, a homogenization approach was proposed in the context of MPP with multi-size perforations. Then, to consider an MPP with a spatial distribution of microperforations, the perforation ratio was introduced as a space-dependent function. Finally, these two models were combined. Experimental measurements were performed to validate the analytical models. The results provide evidence that:

1. MPP with multi-size perforations can broaden the frequency band of the effective added damping. When the perforation diameters are chosen so that each characteristic frequency coincides with a resonance frequency of the MPP, the frequency band of the effective damping is extended.
2. MPP with spatial distribution of perforations can maximize the added damping on a given mode. Indeed, the distribution of perforations around the antinodes of the considered mode maximizes the added damping compared to a homogeneous MPP.
3. The damping effects of the multi-size perforations and the spatial distribution of perforations can be cumulated. The combination of multiple perforation sizes with inhomogeneous spatial distribution of perforations had the two main advantages. The first is to expand the range of frequencies in which the additional damping is effective. The second is to optimize the amount of added damping across a carefully chosen set of frequencies.

In practice, the perforations could be distributed around the vibration antinodes of the plate modeshapes that need to be dampened.

CRediT authorship contribution statement

Lucie Gallerand: Conceptualization, Methodology, Software, Validation, Writing - original draft, Writing - review & editing. **Mathias Legrand**: Conceptualization, Methodology, Supervision, Writing - original draft, review & editing. **Thomas Dupont**: Conceptualization, Methodology, Supervision, Resources, Funding acquisition, Writing - original draft, review & editing. **Raymond Panneton**: Conceptualization, Methodology, Supervision, Writing - original draft, review & editing. **Philippe Leclaire**: Conceptualization, Methodology, Supervision, Writing - original draft, review & editing.

Supplementary material

Python scripts used to perform the modal analysis presented in this article are available in commit 292f7864 of the [Git repository] Inhomogeneous Perforated Plate

Acknowledgment

This work was supported by the Natural Sciences and Engineering Research Council of Canada (NSERC) and by Fonds de recherche du Québec - Nature et technologies (FRQNT) program financing through the project of the reference number RGPIN-2019-06573.

References

[1] T. Adams. *Sound materials: A compendium of sound absorbing materials for architecture and design*. Frame Publishers, 2017. ISBN: 978-94-923-1153-5.

[2] M. Arnold, A. R. Boccaccini, and G. Ondracek. Prediction of the poisson's ratio of porous materials. *Journal of Materials Science*, 31(6):1643–1646, 1996. [DOI].

[3] N. Atalla and F. Sgard. Modeling of perforated plates and screens using rigid frame porous models. *Journal of Sound and Vibration*, 303:195–208, 2007. [DOI], [OA].

[4] M.A. Biot. Theory of propagation of elastic waves in a fluid-saturated porous solid. I. Low-frequency range. *Journal of the Acoustical Society of America*, 28(2):168–178, 1956. [DOI], [OA].

[5] M.A. Biot. Theory of propagation of elastic waves in a fluid-saturated porous solid. II. Higher frequency range. *Journal of the Acoustical Society of America*, 28(2):179–191, 1956. [DOI], [OA].

[6] A.R. Boccaccini and Z. Fan. A new approach for the Young's modulus-porosity correlation of ceramic materials. *Ceramics International*, 23(3):239–245, 1997. [DOI].

[7] T. Bravo, C. Maury, and C. Pinhède. Vibroacoustic properties of thin micro-perforated panel absorbers. *Journal of the Acoustical Society of America*, 132:789–798, 2012. [DOI].

[8] J. Carbajo, J. Ramis, L. Godinho, and P. Amado-Mendes. Assessment of methods to study the acoustic properties of heterogeneous perforated panel absorbers. *Applied Acoustics*, 133:1–7, 2018. [DOI].

[9] J. Carbajo, J. Ramis, L. Godinho, and P. Amado-Mendes. Perforated panel absorbers with micro-perforated partitions. *Applied Acoustics*, 149:108–113, 2019. [DOI].

[10] Y. Champoux and M.R. Stinson. On acoustical models for sound propagation in rigid frame porous materials and the influence of shape factors. *Journal of the Acoustical Society of America*, 92:1120–1131, 1992. [DOI].

[11] T. Dupont, G. Pavic, and B. Laulagnet. Acoustic properties of lightweight micro-perforated plate systems. *Acta Acustica united with Acustica*, 89(2):201–212, 2003. [OA].

[12] ASTM Designation: E756-05(2017). *Standard Test Method for Measuring Vibration-Damping Properties of Materials*. ASTM International, 2017. [DOI].

[13] L. Gallerand, M. Legrand, T. Dupont, and P. Leclaire. Vibration and damping analysis of a thin finite-size microperforated plate. *Journal of Sound and Vibration*, 541:117295, 2022. [DOI], [OA].

[14] K. Hoshi, T. Hanyu, T. Okuzono, K. Sakagami, M. Yairi, S. Harada, S. Takahashi, and Y. Ueda. Implementation experiment of a honeycomb-backed MPP sound absorber in a meeting room. *Applied Acoustics*, 157:107000, 2020. [DOI].

[15] K. H. Kim and G. H. Yoon. Absorption performance optimization of perforated plate using multiple-sized holes and a porous separating partition. *Applied Acoustics*, 120:21–33, 2017. [DOI].

[16] P. Leclaire, K.V. Horoshenkov, and A. Cummings. Transverse vibration of a thin rectangular porous plate saturated by a fluid. *Journal of Sound and Vibration*, 247(1):1–18, 2001. [DOI], [OA].

[17] M. P. Lutz and R. W. Zimmerman. The effect of pore shape on the poisson ratio of porous materials. *Mathematics and Mechanics of Solids*, 26(8):1191–1203, 2021. [DOI].

[18] D.-Y. Maa. Microperforated-panel wideband absorbers. *Noise Control Engineering Journal*, 29(3):77, 1987. [DOI].

[19] L. Maxit, C. Yang, L. Cheng, and J.-L. Guyader. Modeling of micro-perforated panels in a complex vibro-acoustic environment using patch transfer function approach. *Journal of the Acoustical Society of America*, 131(3):2118–2130, 2012. [DOI].

[20] I.M. Miasa, M. Okuma, G. Kishimoto, and T. Nakahara. An Experimental Study of a Multi-Size Microperforated Panel Absorber. *Journal of System Design and Dynamics*, 1(2):331–339, 2007. [DOI].

[21] A.I. Mosa, A. Putra, R. Ramlan, I. Prasetiyo, and A. Esraa. Theoretical model of absorption coefficient of an inhomogeneous MPP absorber with multi-cavity depths. *Applied Acoustics*, 146:409–419, 2019. [DOI].

[22] M. Ouisse, L. Maxit, C. Cacciolati, and J.-L. Guyader. Patch transfer functions as a tool to couple linear acoustic problems. *Journal of Vibration and Acoustics*, 127(5):458–466, 2004. [DOI].

[23] A. Putra, Y. M. Cheah, N. Muhammad, A. Rivai, and C. M. Wai. The effect of perforation on the dynamics of a flexible panel. *Advances in Acoustics and Vibration*, 2014:1–17, 2014. [DOI].

[24] Y. Qian and K. Zhang. Influence of arranged patterns on the absorption performance of parallel MPP absorbers. *Applied Acoustics*, 192:108701, 2022. [DOI].

[25] Y.J. Qian, K. Cui, S.M. Liu, Z.B. Li, D.S. Shao, D.Y. Kong, and S.M. Sun. Optimization of multi-size micro-perforated panel absorbers using multi-population genetic algorithm. *Noise Control Engineering Journal*, 62(1):37–46, 2014. [DOI].

[26] H. Ruiz, P. Cobo, and F. Jacobsen. Optimization of multiple-layer microperforated panels by simulated annealing. *Applied Acoustics*, 72(10):772–776, 2011. [DOI].

[27] D. Takahashi and M. Tanaka. Flexural vibration of perforated plates and porous elastic materials under acoustic loading. *Journal of the Acoustical Society of America*, 112(4):1456–1464, 2002. [DOI].

[28] M.A. Temiz, J. Tournadre, I.L. Arteaga, P. Martínez-Lera, and A. Hirschberg. Modelling vibro-acoustic coupling in flexible micro-perforated plates by a patch-impedance approach. *Applied Acoustics*, 125:80–90, 2017. [DOI].

[29] L. Wang and T. Wang. Investigation of the effect of perforated sheath on thermal-flow characteristics over a gas turbine reverse-flow combustor—Part 2: Computational analysis. *Journal of Thermal Science and Engineering Applications*, 12(4), 2019. [DOI], [OA].

[30] M.Q. Wu. Micro-perforated panels for duct silencing. *Noise Control Engineering Journal*, 45(2):69–77, 1997. [DOI], [OA].

[31] B. Zhang, S. Lang, P. Ge, and W. Zhuang. The study of sound absorption characteristic of micro-perforated panel with different diameter holes. In *29th International Congress and Exhibition on Noise Control Engineering (internoise 2000)*, 2000. [OA].